Isolated MMC-based ac/ac stage for ultrafast chargers

Isolated MMC-based ac/ac stage for ultrafast chargers

Ygor Pereira Marca, Maurice G. L. Roes, Jorge L. Duarte and Korneel G. E. Wijnands
Department of Electrical Engineering, Electromechanics and Power Electronics Group
Eindhoven University of Technology, Eindhoven, The Netherlands
Email: y.pereira.marca@tue.nl

***Abstract*—The application of indirect and direct modular multilevel converter-based topologies in an isolated ultrafast charger, operating from a three-phase medium-voltage grid, is compared. The most promising circuit is an isolated direct ac/ac modular multilevel converter, in which four-quadrant operation is possible by employing full-bridge sub-modules. The direct ac/ac conversion reduces the cost and volume of fast charging stations by eliminating line frequency transformers. An analytical model focusing on the decomposition of circuit states is employed to present the control scheme. Subsequently, the approach is validated with simulation results, corroborating the suitability for high-power bidirectional battery chargers.**

***Index Terms*—battery, full-bridge, isolated, medium-voltage, modular multilevel converter, transformer, ultrafast charger.**

I. Introduction

Charging large vehicles require power levels of 500 kW and above, which calls for the development of ultrafast charging stations. In this case, to quickly charge the electric vehicle battery, a connection to the medium-voltage (MV) grid is commonly required to prevent overloading the distribution grid. Conventional charging stations include a line-frequency (LF) transformer (Fig. 1a) to reduce voltage and provide isolation [1].

Employing a medium-frequency (MF) instead of LF transformer, however, can decrease the charger's cost and volume (Fig. 1b). Combining MF transformers and power electronics remove the demand for a heavy LF transformer. Typical solutions include cascaded H-bridge converters as in [2], [3] or a modular multilevel converter (MMC) [4]. MMCs are typically used in high-voltage direct current (HVDC) systems [5], [6]. Nevertheless, the MMC can also operate to feed a MF transformer [7], [8].

Consequently, to reduce the charger's overall volume, this paper investigates the opportunity of applying an ac/ac MMC to interface a three-phase MV grid to a single-phase MF transformer (Fig. 1b). A comparison of efficiency and component count between a direct ac/ac MMC and indirect ac/dc/ac MMC topologies by modeling the ac/ac stage of a charging station is made in the text.

II. Modular multilevel converter

The MMC has been widely applied for MV and high-power conversion because of advantages such as low total harmonic distortion (THD), modularity and high efficiency [9].

978-1-7281-9023-5/21/$31.00 ©2021 European Union

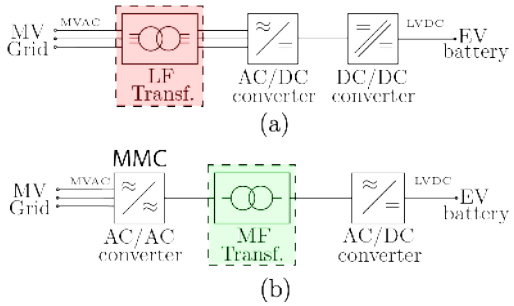

Fig. 1. Architectures of ultrafast charging stations: (a) Charger with line-frequency transformer. (b) Proposed charger based on a MMC and a medium-frequency transformer.

Moreover, the converter easily scales to different voltage and power levels due to its modularity. This paper discusses both the direct ac/ac MMC and indirect ac/dc/ac MMC for ultrafast chargers.

The direct ac/ac MMC consists of three-legs, one for each grid phase (Fig. 2). Each one of these legs is composed of two arms: a lower and an upper arm. The arms are comprised of series-connected sub-modules (SM), which consist of a full-bridge (FB) converters with a dc bus capacitor. FB SMs extend the MMC's operating range, which enables to connect the three-phase MV grid to a single-phase voltage with higher frequency than 50 Hz [7], [8], [10].

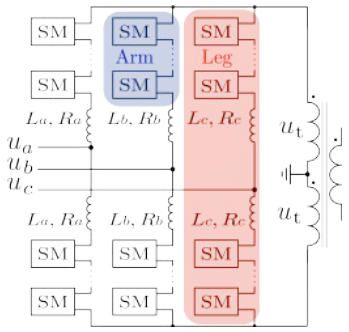

Fig. 2. Direct ac/ac MMC with SMs and single-phase MF transformer.

The indirect ac/dc/ac MMC consists of three-legs on the three-phase side and two-legs on the MF transformer side (Fig. 3). In addition, dc bus capacitors (C_{dc}) are applied to form an intermediate energy buffer. The arms can be composed of

diverse sub-module topologies, which are investigated in next section.

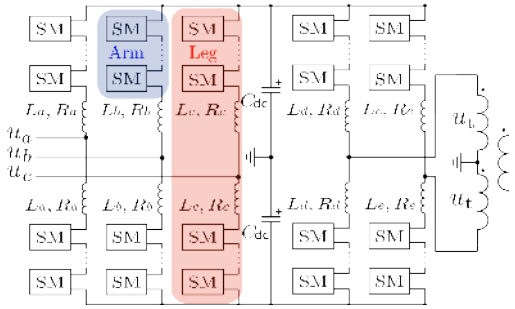

Fig. 3. Indirect ac/dc/ac MMC with SMs and single-phase MF transformer.

III. Three-phase to single-phase MMCs

The two most straightforward configurations of the MMC to perform three-phase to single-phase power conversion are the direct ac/ac (Fig. 5) and indirect ac/dc/ac (Fig. 6) [11]. Most publications regarding the direct ac/ac MMC are applied in railway grids with 16.7 Hz [12]–[14], which require a low-frequency single-phase voltage instead of the medium-frequency that we are aiming for in this paper. However, the ac/ac MMC can directly connect to a MF transformer [7], [8]. This section will compare the direct ac/ac with the indirect ac/dc/ac MMC.

The SMs can be composed as illustrated in Fig. 4 with a stack of FB, half-bridge (HB) or mixed FB and HB converters. The direct ac/ac MMC converter can only use FB SMs (Fig. 4a) since it must operate in four quadrants. The indirect ac/dc/ac, however, can use FB (Fig. 4a), HB (Fig. 4b) and mixed-type (Fig. 4c) SMs. This section aims to calculate the efficiency, number of switches and sub-modules in order to identify the most cost-effective topology for the ac/ac stage.

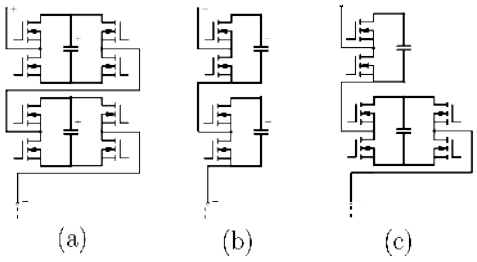

Fig. 4. Sub-module topologies: (a) Full-bridge. (b) Half-bridge. (c) Mixed-type.

A. Direct ac/ac MMC

The direct ac/ac MMC presents six controllable voltage sources located in the upper ($u_a^{\mathrm{u}}, u_b^{\mathrm{u}}, u_c^{\mathrm{u}}$) and lower ($u_a^{\ell}, u_b^{\ell}, u_c^{\ell}$) arms, realized as FB SMs, as presented in Fig. 5.

For each of the three phases indexed with by $y \in \{a,\ b,\ c\}$, there is an upper and a lower arm indicated by $\mathrm{x} \in \{\mathrm{u},\ \ell\}$. As described later on in Section IV, when considering in Fig. 5

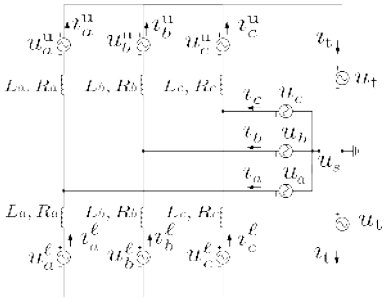

Fig. 5. Direct ac/ac MMC with FB SMs.

balanced sinusoidal waveforms for the three-phase side (with RMS value U_y and peak value $\widehat{U}_y = \sqrt{2}U_y$) and the single-phase side (peak value $\widehat{U}_t$ and RMS value U_t), the required minimum number of SMs per arm is given by

$$N = \left\lceil \frac{\widehat{U}_y + \widehat{U}_t}{\mathrm{V}_{sw}} \right\rceil. \tag{1}$$

where V_{sw} is the derated maximal voltage of the switches. Therefore, the total number of SMs and switches in the direct ac/ac converter are given by

$$N_{(1)}^{sm} = 6N, \tag{2}$$

$$N_{(1)}^{sw} = 24N, \tag{3}$$

respectively. Now, it will be assumed that the converter operates in steady-state and that the single and three-phase currents are in phase with their respective voltages. Additionally, it will assumed that currents circulating between the legs without interaction with the terminals have a negligible contribution to the total RMS current per leg. Therefore, the three-phase power is equal to the single-phase and the single-phase current and the arm current are determine by

$$I_{\mathrm{t}} = \frac{3U_y I_y}{2U_{\mathrm{t}}}. \tag{4}$$

$$I_y^{\mathrm{x}} = \sqrt{\frac{I_y^2}{4} + \frac{I_{\mathrm{t}}^2}{9}}. \tag{5}$$

Total conduction losses of the direct ac/ac MMC can be approximated by

$$P_{\mathrm{loss}(1)} = 12R_{ds}N(I_y^{\mathrm{x}})^2, \tag{6}$$

where Rds is the on-state resistance of each switch of the sub-module (in present-time the switching losses in power semiconductor devices are less dominant, being therefore not included in the subsequent analysis for simplification).

B. Indirect ac/dc/ac MMC

The indirect ac/dc/ac converter is composed of an ac/dc MMC to interface the thee-phase MV grid with a dc bus and an ac/dc MMC with two legs to convert the DC bus voltage into a single-phase voltage, as presented in Fig. 6.

Assuming no losses it follows that

$$I_{dc} = \frac{3U_y I_y}{2U_{dc}}. \tag{7}$$

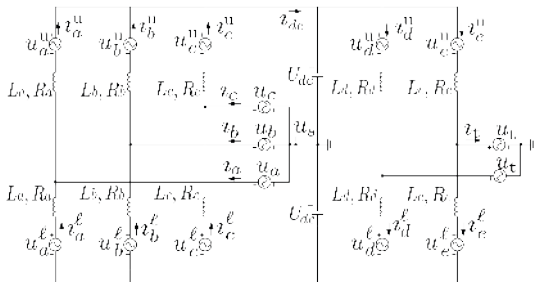

Fig. 6. Indirect ac/dc/ac MMC with FB, HB or mixed SMs.

The two legs of the single-phase MMC are indicated by $z \in \{d,\, e\}$. The RMS current in each arm of the three-phase and single-phase sides are found to be

$$I_y^{\mathrm{x}} = \sqrt{\frac{I_y^2}{4} + \frac{I_{dc}^2}{9}}, \quad (8) \qquad I_z^{\mathrm{x}} = \sqrt{\frac{I_{\mathrm{t}}^2}{4} + \frac{I_{dc}^2}{4}}. \quad (9)$$

The power losses, number of switches and power efficiency of HB, FB and mixed-type SMs are considered in the following.

1) HB SMs: The number of half-bridge SMs per arm in the three-phase and single-phase MMCs are determined as

$$N_y = \left\lceil \frac{\widehat{U}_y + U_{dc}}{\mathrm{V}_{sw}} \right\rceil, \quad (10) \qquad N_z = \left\lceil \frac{\widehat{U}_{\mathrm{t}} + U_{dc}}{\mathrm{V}_{sw}} \right\rceil, \quad (11)$$

respectively, the total number of SMs and switches of this configuration are expressed as

$$N_{(2)}^{sm} = 6N_y + 4N_z, \quad (12) \qquad N_{(2)}^{sw} = 12N_y + 8N_z. \quad (13)$$

The total conduction losses of the indirect ac/dc/ac MMC with HB SMs is given by

$$P_{\mathrm{loss}(2)} = 6R_{ds}N_y(I_y^{\mathrm{x}})^2 + 4R_{ds}N_z(I_z^{\mathrm{x}})^2. \quad (14)$$

2) FB SMs: The number of FB SMs per arm is equal to HB SMs. As a result

$$N_{(3)}^{sm} = N_{(2)}^{sm}, \quad (15) \qquad N_{(3)}^{sw} = 2N_{(2)}^{sw}, \quad (16)$$

and the total conduction losses of the indirect ac/dc/ac MMC with FB SMs are determined by

$$P_{\mathrm{loss}(3)} = 12R_{ds}N_y(I_y^{\mathrm{x}})^2 + 8R_{ds}N_z(I_z^{\mathrm{x}})^2. \quad (17)$$

3) Mixed SMs: The mixed-type configuration (Fig. 4c) has both half- and full-bridges. FB SMs are necessary when the sub-modules should be able to make a negative voltage. This occurs when U_{dc} is lower than $\widehat{U}_y$ or $\widehat{U}_{\mathrm{t}}$. By only using the minimum number of required FB modules for supplying this negative voltage and using HB modules for the rest of the arm, considerable savings in losses and number of switched can be obtained. First, the number of FB SMs per arm in the MMC's three-phase and single-phase sides are found to be

$$N_y^{\mathrm{FB}} = \max\left(\left\lceil \frac{\widehat{U}_y - U_{dc}}{\mathrm{V}_{sw}} \right\rceil, 0\right), \quad (18)$$

$$N_z^{\mathrm{FB}} = \max\left(\left\lceil \frac{\widehat{U}_{\mathrm{t}} - U_{dc}}{\mathrm{V}_{sw}} \right\rceil, 0\right). \quad (19)$$

Then, the number of HB SMs per arm in both sides follows from

$$N_y^{\mathrm{HB}} = N_y - N_y^{\mathrm{FB}}, \quad (20)$$

$$N_z^{\mathrm{HB}} = N_z - N_z^{\mathrm{FB}}. \quad (21)$$

The total number of SMs and switches is expressed as

$$N_{(4)}^{sm} = 6N_y^{\mathrm{FB}} + 4N_z^{\mathrm{FB}} + 6N_y^{\mathrm{HB}} + 4N_z^{\mathrm{HB}}. \quad (22)$$

$$N_{(4)}^{sw} = 24N_y^{\mathrm{FB}} + 16N_z^{\mathrm{FB}} + 12N_y^{\mathrm{HB}} + 8N_z^{\mathrm{HB}}, \quad (23)$$

Finally the conduction losses in the ac/dc/ac MMC with hybrid SMs is then

$$\begin{aligned} P_{\mathrm{loss}(4)} = {} & 12R_{ds}N_y^{\mathrm{FB}}(I_y^{\mathrm{x}})^2 + 8R_{ds}N_z^{\mathrm{FB}}(I_z^{\mathrm{x}})^2 + \cdots \\ & 6R_{ds}N_y^{\mathrm{HB}}(I_y^{\mathrm{x}})^2 + 4R_{ds}N_z^{\mathrm{HB}}(I_z^{\mathrm{x}})^2. \end{aligned} \quad (24)$$

C. Comparison

The four cases (1:Direct ac/ac MMC with FB SMs, 2:Indirect ac/dc/ac MMC with HB SMs, 3:Indirect ac/dc/ac MMC with FB SMs, 4:Indirect ac/dc/ac MMC with mixed SMs) are compared in the following regarding efficiency, number of sub-modules and switches. While the efficiency and number of switches are related, increasing the number of sub-modules also adds capacitors, auxiliary circuits and communication to the charger.

With the four cases indexed with $\nu \in \{1,\, 2,\, 3,\, 4,\}$, the power efficiency for each case is estimated with

$$\eta_\nu = \left(1 - \frac{P_{\mathrm{loss}(\nu)}}{P_{ac}}\right) \cdot 100, \quad (25)$$

where P_{ac} is the charger's nominal processed power as given in Table I.

TABLE I
HIGH-POWER, MEDIUM-VOLTAGE CHARGER RATINGS.

Description	Variable	Value	Unit
Charger nominal power	P_{ac}	1	MW
MV phase-to-neutral RMS voltage	U_y	$25\sqrt{1/3}$	kV
MOSFET breakdown voltage	V_{ds}	1.2	kV
MOSFET derating factor	D_F	75	%
MOSFET on-resistance	R_{ds}	20	mΩ

Note that switching losses are disregarded by employing 1.2kV SiC MOSFETs and that a moderate derating factor is considered for the switches' rated voltage, yielding a practical maximum voltage level for application purposes given by

$$\mathrm{V}_{sw} = \mathrm{V}_{ds}D_F. \quad (26)$$

There are two degrees of freedom for choosing a compromise between system efficiency and number of devices, the dc bus voltage (U_{dc}) for the indirect ac/dc/ac MMCs and the single-phase voltage (U_{t}) for the four cases. However, if $U_{dc} \geq \widehat{U}_y$, mixed-type sub-modules may be composed only of HBs, so it is considered out of the scope of this paper as the result is the same as for case 2.

The variables of interest in (2), (3), (13), (12), (16), (15), (23), (22) and (25) are plotted in relation to single-phase transformer voltage. The first comparison is made with $U_{dc} = \widehat{U}_y$ as shown in Fig. 7a. The efficiency and number of switches of both cases 1 and 2 are comparable, but the reduced number of sub-modules of case 1 is favorable.

The other comparisons are performed when $U_{dc} < \widehat{U}_y$, for instance $U_{dc} = \frac{\widehat{U}_y}{2}$ (Fig. 7b) and $U_{dc} = \frac{\widehat{U}_y}{10}$ (Fig. 7c). Note that converter arms with only HB SMs cannot operate when $U_{dc} < \widehat{U}_y$, so it is not considered. While the low number of SMs in case 1 is an advantage (Fig. 7b), the efficiencies are similar. When the dc bus voltage is greatly reduced (Fig. 7c), the number of SMs and switches are similar, but the ac/dc/ac converter efficiency drops. In view of the results in Fig. 7, the direct ac/ac MMC is more advantageous than the indirect ac/dc/ac MMC for ultrafast charger when both have the same number of SMs.

IV. MMC FUNDAMENTALS

It is convenient to simplify the converter modeling to an averaged equivalent circuit [15]. The model is useful to simulate the MMC operation without applying insertion and having to balance the capacitors of each SM. In this model, the SMs are represented by controllable average voltage sources without switches, as shown in Fig. 8 [16]. To prevent short-circuit and to allow control of the currents, each arm has a series inductance.

Considering equal inductance and resistance in each arm (Fig. 5), Kirchhoff's voltage law applied to the upper and lower loops results in

$$L_y \frac{\mathrm{d}}{\mathrm{d}\,t} \imath_y^{\mathrm{u}} + R_y \imath_y^{\mathrm{u}} = u_y^{\mathrm{u}} + u_y + u_s - u_{\mathrm{t}}, \tag{27}$$

$$L_y \frac{\mathrm{d}}{\mathrm{d}\,t} \imath_y^{\ell} + R_y \imath_y^{\ell} = u_y^{\ell} - u_y - u_s - u_{\mathrm{t}}. \tag{28}$$

The controllable arm voltage sources are based on the connection in series of N FB SMs (Fig. 4a). The arm voltage (u_y^{x}) is synthesized by the SMs from their capacitor voltages $\mathrm{v}_{y,k}^{\mathrm{x}}$. The arm voltage is related to them by

$$u_y^{\mathrm{x}} = \sum_{k=1}^{N} S_{y,k}^{\mathrm{x}}\, \mathrm{v}_{y,k}^{\mathrm{x}}, \tag{29}$$

$$\mathrm{v}_y^{\mathrm{x}} = \sum_{k=1}^{N} \mathrm{v}_{y,k}^{\mathrm{x}}, \tag{30}$$

with the k^{th} SM's switching function given by $S_{y,k}^{\mathrm{x}} \in \{-1, 0, 1\}$. The summed capacitor voltage $\mathrm{v}_y^{\mathrm{x}}$ is also indicated in the equivalent circuit of Fig. 8. Assuming that the capacitor voltage is equal for every module in the arm, u_y^{x} can be steered by an average insertion index n_y^{x} as

$$u_y^{\mathrm{x}} = n_y^{\mathrm{x}} \mathrm{v}_y^{\mathrm{x}}, \tag{31}$$

$$n_y^{\mathrm{x}} = \frac{1}{N} \sum_{k=1}^{N} S_{y,k}^{\mathrm{x}}, \tag{32}$$

where $-1 \leq n_y^{\mathrm{x}} \leq 1$. Assuming that the capacitors in each arm equal and connected in series, the equivalent arm capacitance reduces as the number of SMs escalates, $C_\sigma = \frac{C_y}{N}$. In addition, for both upper and lower arms, the arm current and the capacitor current are related through the arm's insertion index. This relation is indicated in Fig. 8 by the controlled current sources for each arm, that drive the capacitor current as

$$\imath_{Cy}^{\mathrm{x}} = -C_\sigma \frac{d}{dt} \mathrm{v}_y^{\mathrm{x}} = n_y^{\mathrm{x}} \imath_y^{\mathrm{x}}. \tag{33}$$

Therefore, the definitions in (31) and (33) are used to model the average switching action of the semiconductor devices with dependent voltage and current sources, as shown in Fig. 8.

The summed capacitor voltage become unstable if insertion indices are adopted without any stabilization control [16]. Therefore, to balance $\mathrm{v}_y^{\mathrm{x}}$ in Fig. 8 a stabilizing control scheme is introduced in section VII.

V. DECOMPOSITION OF THE CIRCUIT STATES

There are ten measurable currents in the circuit of Fig. 8; namely the currents through the upper arms ($\imath_a^{\mathrm{u}}, \imath_b^{\mathrm{u}}, \imath_c^{\mathrm{u}}$), lower arms ($\imath_a^{\ell}, \imath_b^{\ell}, \imath_c^{\ell}$), three-phase grid lines ($\imath_a, \imath_b, \imath_c$), and single-phase MF transformer ($\imath_{\mathrm{t}}$). Due to Kirchoff's current law, any set of five out of these ten currents can be freely chosen, the remaining ones are dependent. Therefore, a keen choice of five currents are obtained by the decomposition of the voltages and currents into the common-mode (Σ) in red and differential-mode (Δ) components in blue:

$$u_y^{\Sigma} = \frac{1}{2}\left[u_y^{\mathrm{u}} + u_y^{\ell}\right], \tag{34}$$

$$\imath_y^{\Sigma} = \frac{1}{2}\left[\imath_y^{\mathrm{u}} + \imath_y^{\ell}\right], \tag{35}$$

$$u_y^{\Delta} = \frac{1}{2}\left[u_y^{\mathrm{u}} - u_y^{\ell}\right], \tag{36}$$

$$\imath_y^{\Delta} = \frac{1}{2}\left[\imath_y^{\mathrm{u}} - \imath_y^{\ell}\right]. \tag{37}$$

Thus, substitution of (34), (35), (36) and (37) into (27) and (28) leads to

$$L_y \frac{\mathrm{d}}{\mathrm{d}\,t} \imath_y^{\Sigma} + R_y \imath_y^{\Sigma} = u_y^{\Sigma} - u_{\mathrm{t}}, \tag{38}$$

$$L_y \frac{\mathrm{d}}{\mathrm{d}\,t} \imath_y^{\Delta} + R_y \imath_y^{\Delta} = u_y^{\Delta} + u_y + u_s. \tag{39}$$

Since there is no connection between the star-point and the ground in Fig. 5, the star-point voltage (u_s) can be different from zero whereas the star-point current $\imath_s = 0$.

Converting the three-phase quantities into an orthogonal space eliminates cross-coupling terms. This can be achieved through the amplitude-invariant Clarke transformation. This transformation consists of a matrix

$$\mathbf{T} = \begin{pmatrix} \frac{2}{3} & -\frac{1}{3} & -\frac{1}{3} \\ 0 & \frac{\sqrt{3}}{3} & -\frac{\sqrt{3}}{3} \\ \frac{1}{3} & \frac{1}{3} & \frac{1}{3} \end{pmatrix} \tag{40}$$

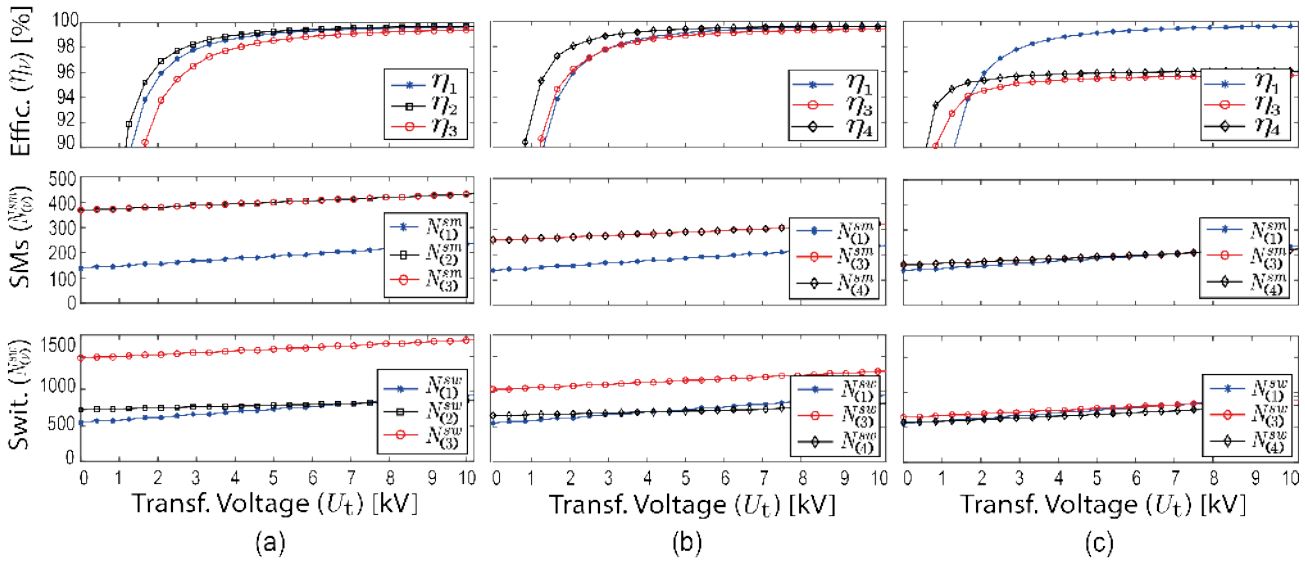

Fig. 7. Comparison between ac/ac and ac/dc/ac MMCs: (a) $U_{dc} = \widehat{U}_y$. (b) $U_{dc} = \frac{\widehat{U}_y}{2}$. (c) $U_{dc} = \frac{\widehat{U}_y}{10}$.

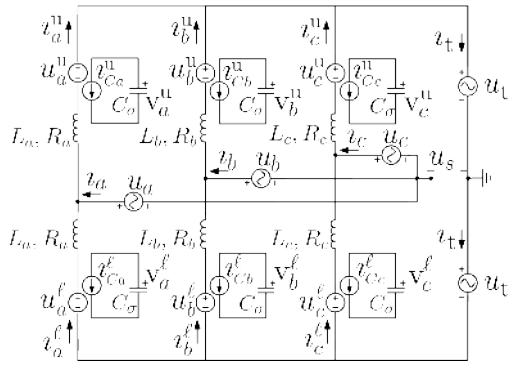

Fig. 8. Direct ac/ac MMC averaged equivalent circuit.

that converts three-phase voltages and currents into the $\alpha\beta\gamma$ stationary reference frame. Introducing vectors as $[\boldsymbol{u}_y]^\top = [u_a\ u_b\ u_c]^\top$, the following definitions based on (40) hold:

$$[u_\alpha\ u_\beta\ u_\gamma]^\top = \mathbf{T}\,[\boldsymbol{u}_y]^\top\ ,\quad [\imath_\alpha\ \imath_\beta\ \imath_\gamma]^\top = \mathbf{T}\,[\boldsymbol{\imath}_y]^\top\ , \tag{41}$$

$$\left[u_\alpha^\Delta\ u_\beta^\Delta\ u_\gamma^\Delta\right]^\top = \mathbf{T}\,\left[\boldsymbol{u}_y^\Delta\right]^\top, \left[\imath_\alpha^\Delta\ \imath_\beta^\Delta\ \imath_\gamma^\Delta\right]^\top = \mathbf{T}\,\left[\boldsymbol{\imath}_y^\Delta\right]^\top, \tag{42}$$

$$\left[u_\alpha^\Sigma\ u_\beta^\Sigma\ u_\gamma^\Sigma\right]^\top = \mathbf{T}\,\left[\boldsymbol{u}_y^\Sigma\right]^\top,\ \left[\imath_\alpha^\Sigma\ \imath_\beta^\Sigma\ \imath_\gamma^\Sigma\right]^\top = \mathbf{T}\,\left[\boldsymbol{\imath}_y^\Sigma\right]^\top. \tag{43}$$

A balanced grid voltage system implies that $u_a + u_b + u_c = 0$, and (41) result in $u_\gamma = 0$ and $\imath_\gamma = 0$. Since the differential-mode current components are related to the three-phase grid ($\imath_y = 2\imath_y^\Delta$), (42) results in $\imath_\gamma^\Delta = 0$. The common-mode components u_γ^Σ and $\imath_\gamma^\Sigma$ from (43) are associated with the single-phase side quantities, as shown in the next section.

VI. Bidirectional Power Flow

This section describes the bidirectional active and reactive power exchange between the three-phase and single-phase terminals which determine the current setpoints to be supplied to the closed-loop controllers.

A. Power exchange with the grid

The *p-q* theory for three-phase systems is commonly applied to define instantaneous real and imaginary power [17]. Considering the amplitude-invariant Clarke transformation in (40) and the differential-mode currents, the instantaneous active and reactive power exchange with the AC grid is given by

$$\begin{bmatrix} P_{\mathrm{AC}} \\ Q_{\mathrm{AC}} \end{bmatrix} = 3 \begin{bmatrix} u_\alpha & u_\beta \\ u_\beta & -u_\alpha \end{bmatrix} \begin{bmatrix} \imath_\alpha^\Delta \\ \imath_\beta^\Delta \end{bmatrix}. \tag{44}$$

Then, for desired reference values of active and reactive power exchange (P_{AC}^* and Q_{AC}^*), it follows from (44) that

$$\begin{bmatrix} \imath_\alpha^{\Delta *} \\ \imath_\beta^{\Delta *} \end{bmatrix} = \frac{1}{u_\alpha^2 + u_\beta^2} \begin{bmatrix} u_\alpha & u_\beta \\ u_\beta & -u_\alpha \end{bmatrix} \frac{1}{3} \begin{bmatrix} P_{\mathrm{AC}}^* \\ Q_{\mathrm{AC}}^* \end{bmatrix}, \tag{45}$$

where $\imath_\alpha^{\Delta *}$ and $\imath_\beta^{\Delta *}$ denote the setpoints for $\imath_\alpha^\Delta$ and $\imath_\beta^\Delta$ in closed control loop, required to reach P_{AC}^* and Q_{AC}^*.

Finally, it is relevant to observe that applying (40) to (39) results in

$$L \frac{\mathrm{d}}{\mathrm{d}\,t} \begin{bmatrix} \imath_\alpha^\Delta \\ \imath_\beta^\Delta \\ 0 \end{bmatrix} + R \begin{bmatrix} \imath_\alpha^\Delta \\ \imath_\beta^\Delta \\ 0 \end{bmatrix} = \begin{bmatrix} u_\alpha^\Delta \\ u_\beta^\Delta \\ u_\gamma^\Delta \end{bmatrix} + \begin{bmatrix} u_\alpha \\ u_\beta \\ u_s \end{bmatrix}. \tag{46}$$

Therefore, the control loops of $\imath_\alpha^\Delta$ and $\imath_\beta^\Delta$ for reaching $\imath_\alpha^{\Delta *}$ and $\imath_\beta^{\Delta *}$ can use u_α^Δ and u_β^Δ as control inputs. Moreover, these control loops are completely decoupled. The implementation of the control of $\imath_\alpha^\Delta$ and $\imath_\beta^\Delta$ is not discussed in this paper, but can for example be achieved in the dq0−reference frame through traditional control methods. Furthermore, (46) reveals

that the star-point voltage (u_s) does not modify the differential-mode currents. Hence, it can be freely assigned through u_γ^Δ for other purposes, for instance to inject a third harmonic component into u_s to increase the converter's voltage range.

B. Power exchange with the MF transformer

The bidirectional active power exchange with the single-phase MF transformer terminals is governed by current $\imath_\mathrm{t}$. As presented in Fig. 8, $\imath_\mathrm{t} = \imath_a^\mathrm{u} + \imath_b^\mathrm{u} + \imath_c^\mathrm{u} = \imath_a^\ell + \imath_b^\ell + \imath_c^\ell$, and applying (34)−(37) results in

$$\imath_\mathrm{t} = (\imath_a^\Sigma + \imath_a^\Delta) + (\imath_b^\Sigma + \imath_b^\Delta) + (\imath_c^\Sigma + \imath_c^\Delta). \tag{47}$$

Since $\imath_a^\Delta + \imath_b^\Delta + \imath_c^\Delta = 0$,

$$\imath_\mathrm{t} = \imath_a^\Sigma + \imath_b^\Sigma + \imath_c^\Sigma, \tag{48}$$

and from (43) we have

$$\imath_\mathrm{t} = 3\,\imath_\gamma^\Sigma. \tag{49}$$

Now, combining (40) and (38) gives

$$L\frac{\mathrm{d}}{\mathrm{d}\,t}\begin{bmatrix}\imath_\alpha^\Sigma\\ \imath_\beta^\Sigma\\ \imath_\gamma^\Sigma\end{bmatrix} + R\begin{bmatrix}\imath_\alpha^\Sigma\\ \imath_\beta^\Sigma\\ \imath_\gamma^\Sigma\end{bmatrix} = \begin{bmatrix}u_\alpha^\Sigma\\ u_\beta^\Sigma\\ u_\gamma^\Sigma\end{bmatrix} - \begin{bmatrix}0\\ 0\\ u_\mathrm{t}\end{bmatrix}. \tag{50}$$

From (50) it is possible to see that u_γ^Σ can perform decoupled control of $\imath_\gamma^\Sigma$. In addition, the generated single-phase voltage and current denoted as

$$\begin{aligned} u_\mathrm{t} &= \widehat{U}_\mathrm{t}\sin(2\pi f_\mathrm{t} t) \\ \imath_\mathrm{t} &= \widehat{I}_\mathrm{t}\sin(2\pi f_\mathrm{t} t - \varphi_\mathrm{t}) \end{aligned} \tag{51}$$

determine the reactive power exchange through the MF transformer, where f_t is the frequency of the transformer voltage. The parameters in (51) can be freely selected, for example to have unitary power factor. In general, the desired active and reactive powers at the single-phase side are chosen with

$$\begin{aligned} S_\mathrm{t}^* &= 2U_\mathrm{t}I_\mathrm{t}^* = 6U_\mathrm{t}I_\gamma^{\Sigma *} \\ P_\mathrm{t}^* &= S_\mathrm{t}^*\cos(\varphi_\mathrm{t}) \\ Q_\mathrm{t}^* &= S_\mathrm{t}^*\sin(\varphi_\mathrm{t}). \end{aligned} \tag{52}$$

Therefore, the power exchange between the MMC and the transformer is controlled by u_γ^Σ, because this voltage component can independently control $\imath_\gamma^\Sigma$ and therefore it according to (50). Lastly, u_α^Σ and u_β^Σ are responsible for the internally circulating currents ($\imath_\alpha^\Sigma$ and $\imath_\beta^\Sigma$).

VII. MMC CONTROL

The scheme proposed here is based in [14], which controls both the active and reactive power exchange with three-phase ac grid, and the summed capacitor voltage. The control does not consider the balancing of capacitor voltages within one arm, for which various methods are available [19], [20]. Therefore, the number of sub-modules is not relevant in the control scheme.

As detailed in [21], the higher-level control can be performed with a PQ controller to generate the voltage references $u_\alpha^{\Delta *}$ and $u_\beta^{\Delta *}$, while $u_\gamma^{\Delta *}$ is a degree of freedom, as shown in Fig. 9. In addition, $u_\gamma^{\Sigma *}$ is feed-forwarded with u_t because the single-phase voltage exchanges power with $\imath_\gamma^\Sigma$. The voltage components $u_\alpha^{\Sigma *}$ and $u_\beta^{\Sigma *}$ can be used to diminish capacitor voltage ripple.

The summed capacitor voltage control proposed here generates six voltage components ($u_\alpha^{\Sigma\ddagger}$, $u_\beta^{\Sigma\ddagger}$, $u_\gamma^{\Sigma\ddagger}$, $u_\alpha^{\Delta\ddagger}$, $u_\beta^{\Delta\ddagger}$ and $u_\gamma^{\Delta\ddagger}$) that are added to $u_\alpha^{\Sigma *}$, $u_\beta^{\Sigma *}$, $u_\gamma^{\Sigma *}$, $u_\alpha^{\Delta *}$, $u_\beta^{\Delta *}$ and $u_\gamma^{\Delta *}$. These components are introduced to slightly change the insertion indices so that voltage unbalance between arms can be compensated [16].

A. Summed capacitor voltage control

The measured summed of capacitor voltages can be decomposed into sum and difference components as

$$\mathbf{v}_y^\Sigma = \frac{1}{2}\left[\mathbf{v}_y^\mathrm{u} + \mathbf{v}_y^\ell\right], \tag{53}$$

$$\mathbf{v}_y^\Delta = \frac{1}{2}\left[\mathbf{v}_y^\mathrm{u} - \mathbf{v}_y^\ell\right]. \tag{54}$$

For a given reference capacitor voltage (v_ref), the following definitions are valid for all circuit phases:

$$\mathrm{v}_y^{\Sigma *} = \mathrm{v}_\mathrm{ref}, \tag{55}$$

$$\mathrm{v}_y^{\Delta *} = 0. \tag{56}$$

A straightforward way to enforce (55) and (56) is to introduce two stabilizing proportional gains K^Σ and K^Δ to reduce the internal capacitor voltage imbalances (Fig. 9) by correcting the error between the measured summed capacitor voltage with v_ref. The controllers of $\mathbf{v}_y^\Sigma$ and $\mathbf{v}_y^\Delta$ determine the magnitude of additional ac components in the frequencies f_t (single-phase side) and f (three-phase side), respectively, which are needed to adjust the capacitor voltages.

According to [14], the component in f_t should be

$$\boldsymbol{u}_y^{\Sigma\ddagger} = K^\Sigma\left(\mathbf{v}_y^\Sigma - \mathrm{v}_\mathrm{ref}\right)\frac{u_\gamma^{\Sigma *}}{\widehat{U}_\mathrm{t}}H_y^\Sigma(s), \tag{57}$$

and the component in f should be

$$\boldsymbol{u}_y^{\Delta\ddagger} = K^\Delta\left(\mathbf{v}_y^\Delta - 0\right)\frac{-\boldsymbol{u}_y}{\widehat{U}_y}H_y^\Delta(s), \tag{58}$$

as shown in Fig. 9. With regard to (50), the closed-loop-system that controls the single-phase current sets the bandwidth to ϖ^γ as

$$u_\gamma^{\Sigma *} = \varpi^\gamma L_y\left(\imath_\gamma^{\Sigma *} - \imath_\gamma^\Sigma\right) - u_\mathrm{t}, \tag{59}$$

where the transformer current reference is derived from (52) as

$$\imath_\gamma^{\Sigma *} = \frac{S_\mathrm{t}^*}{6U_\mathrm{t}^*}\sin(2\pi f_\mathrm{t} t + \phi - \varphi_\mathrm{t}), \tag{60}$$

where ϕ is an arbitrary angle used to control the power transfer (not covered in this paper).

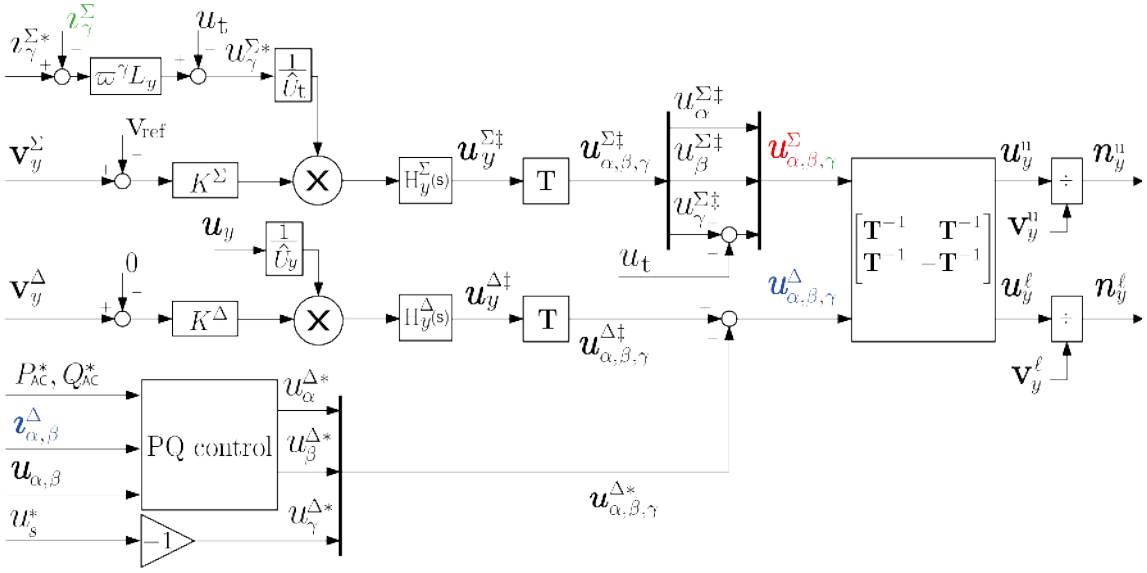

Fig. 9. Control scheme of the three-phase ac/ac MMC.

Furthermore, as also presented in [14], the control scheme includes band-pass filters H_y^{Σ} and H_y^{Δ} with bandwidths ϖ^{Σ} and ϖ^{Δ} centered at f_{t} and f as

$$H_y^{\Sigma}(s) = \frac{\varpi^{\Sigma} s}{s^2 + \varpi^{\Sigma} s + (2\pi f_{\mathrm{t}})^2},$$
$$H_y^{\Delta}(s) = \frac{\varpi^{\Delta} s}{s^2 + \varpi^{\Delta} s + (2\pi f)^2}, \tag{61}$$

to emphasize the desirable frequencies that compose the controllable arm voltages. Next, applying (40) leads to the setpoints $u_{\alpha}^{\Sigma\ddagger}$, $u_{\beta}^{\Sigma\ddagger}$, $u_{\gamma}^{\Sigma\ddagger}$, $u_{\alpha}^{\Delta\ddagger}$, $u_{\beta}^{\Delta\ddagger}$ and $u_{\gamma}^{\Delta\ddagger}$ that create the six decoupled voltages (u_{α}^{Σ}, u_{β}^{Σ}, u_{γ}^{Σ}, u_{α}^{Δ}, u_{β}^{Δ} and u_{γ}^{Δ}). As shown in Fig. 9,

$$\left[u_{\alpha}^{\Sigma}\ u_{\beta}^{\Sigma}\ u_{\gamma}^{\Sigma}\right]^{\top} = \left[u_{\alpha}^{\Sigma\ddagger}\ u_{\beta}^{\Sigma\ddagger}\ u_{\gamma}^{\Sigma\ddagger}\right]^{\top} + \left[0\ 0\ u_{\mathrm{t}}\right]^{\top}, \tag{62}$$

$$\left[u_{\alpha}^{\Delta}\ u_{\beta}^{\Delta}\ u_{\gamma}^{\Delta}\right]^{\top} = \left[u_{\alpha}^{\Delta\ddagger}\ u_{\beta}^{\Delta\ddagger}\ u_{\gamma}^{\Delta\ddagger}\right]^{\top} + \left[u_{\alpha}^{\Delta *}\ u_{\beta}^{\Delta *}\ u_{\gamma}^{\Delta *}\right]^{\top}, \tag{63}$$

which demonstrates the application of the controller outputs to generate differential-mode and common-mode voltages.

Finally, the controllable arm voltages are derived from the inverse Clarke transformation ($\mathbf{T}^{-1}$) (Fig. 9), which leads to the insertion indices as presented in (31). These indices are applied to drive the circuit in Fig. 8.

VIII. Simulations Results

To verify the MMC control scheme operation, simulations were conducted with the parameters from Tables I and II.

In the simulations $P_{\mathrm{t}}^{*} = P_{ac}^{*}$ and $Q_{\mathrm{t}}^{*} = 0$ are considered to calculate the transformer current reference, and $u_s^{*} = 0$ is chosen (Fig. 9). Furthermore, the common-mode and differential-mode controller gains are set as $K^{\Sigma} = 0.5$ and $K^{\Delta} = 1$. The simulation results in Fig. 10 show that the summed capacitor voltage stabilize around the reference ($\mathrm{v_{ref}} = \widehat{U}_{\mathrm{t}} + \widehat{U}_y$), contain both f and f_{t} components and have a small voltage ripple due to the medium-frequency circulating currents. The (upper) arm voltages also contain both frequencies since they have to interface the grid and MF transformer.

TABLE II
Ratings of the Simulated Direct AC/AC MMC with FB SMs.

Description	Variable	Value	Unit
Charger active power reference	P_{ac}^{*}	1	MW
Charger reactive power reference	Q_{ac}^{*}	1	kVAr
Single-phase transformer RMS voltage	U_{t}	5	kV
Grid frequency	f	50	Hz
Transformer frequency	f_{t}	1000	Hz
Equivalent arm capacitance	C_{σ}	1	mF
Arm inductance	L_y	1	mH
Arm resistance	R_y	0.01	Ω
Common-mode filter bandwidth	ϖ^{Σ}	20	rad/s
Differential-mode filter bandwidth	ϖ^{Δ}	20	rad/s
Single-phase current controller bandwidth	ϖ^{γ}	500	rad/s

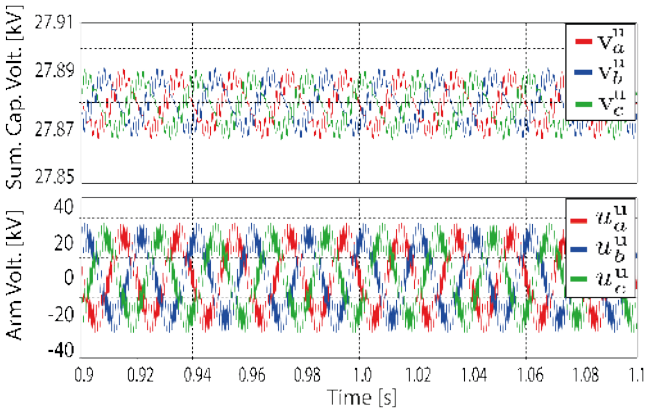

Fig. 10. Simulated voltage waveforms during steady-state operation: Upper arms summed capacitor voltage and upper arm voltages.

Finally, the charger operation is verified through the response of the currents to a step in P^*_{ac} (Fig. 11). The step given through the PQ controller (Fig. 9) immediately increases the three-phase ac currents, which cause the MF transformer and arm currents to adjust to the new current.

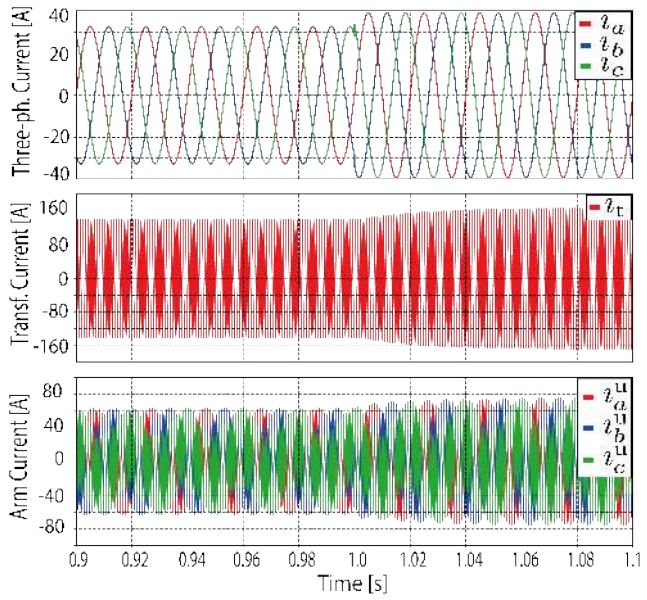

Fig. 11. Simulated current waveforms during a step change in the active power reference, which is increased by 20% at $t = 1s$: Three-phase grid currents, MF transformer current and upper arm currents.

IX. Conclusion

The FB-based ac/ac MMC is able to remove the bulky LF transformer from conventional chargers, reducing cost and volume. Moreover, the isolated stage requires less magnetic components than a cascaded H-bridge converter. The ac/ac MMC needs less SMs and has a higher efficiency in comparison to an indirect ac/dc/ac MMC.

The presented modeling method, where six input voltages can be used to control five currents in a decoupled way, allows a degree of freedom for additional features.

Simulations show that the control scheme is able to balance the arm capacitor voltages while imposing the input and output power. The interaction between the three-phase and single-phase input/output quantities introduce the fundamental frequencies from both sides in the MMC variables. However, other harmonic components are also generated by the proposed control algorithm. This will be analyzed in a future paper.

X. Acknowledgment

The authors would like to thank the NEON (New Energy and mobility Outlook for the Netherlands) research team and partners for their support and helpful suggestions.

References

[1] S. Srdic and S. Lukic, "Toward extreme fast charging: Challenges and opportunities in directly connecting to medium-voltage line," IEEE Electrification Magazine, vol.7, no. 1, pp. 22-31, March 2019.

[2] M. Vasiladiotis, A. Rufer, and A. Beguin, "Modular converter architecture for medium voltage ultra fast EV charging Stations: Global system considerations," IEEE International Electric Vehicle Conference (IEVC), Mar. 2012, pp. 1–7.

[3] H. Tu, H. Feng, S. Srdic, and S. Lukic, "Extreme fast charging of electric vehicles: a technology overview," IEEE Transactions on Transportation Electrification, vol.5, no. 4, pp. 861-878, Dec. 2019.

[4] Z. Pi, P. Wang, Z. Chu, H. Zhu, Z. Sun and Y. Li, "A three-phase 10 kVAC-750 VDC power electronic transformer for smart distribution grid," European Conference on Power Electronics and Applications (EPE), Sept. 2013, pp. 1-9.

[5] W. Lin, D. Jovcic, S. Nguefeu, H. Saad, "Full-bridge MMC converter optimal design to HVDC operational requirements," IEEE Transactions on Power Delivery, vol. 31, no. 3, pp. 1342–1350, June 2016.

[6] P. Bakas, Y. Okazaki, A. Shukla, S. K. Patro, K. Ilves, F. Dijkhuizen and A. Nami, "Review of Hybrid Multilevel Converter Topologies Utilizing Thyristors for HVDC Applications," IEEE Transactions on Power Electronics, vol. 36, no. 1, pp. 174-190, January 2021.

[7] M. Glinka and R. Marquardt, "A new AC/AC-multilevel converter family applied to a single-phase converter," The Fifth International Conference on Power Electronics and Drive Systems (PEDS), vol. 1, Nov. 2003.

[8] M. Glinka and R. Marquardt, "A new AC/AC multilevel converter family," IEEE Transactions on Industrial Electronics, vol. 52, no. 3, pp. 662-669, May 2005.

[9] A. Lesnicar and R. Marquardt, "An innovative modular multilevel converter topology suitable for a wide power range," IEEE Bologna PowerTech Conference Proceedings, vol. 3, pp. 1-6, June 2003.

[10] K. Sharifabadi, L. Harnefors, H.-P. Nee, R. Teodorescu, and S. Norrga, Design, "Control and Application of Modular Multilevel Converters for HVDC Transmission Systems," Hoboken, NJ, USA: Wiley, 2016.

[11] I. Krastev, P. Tricoli, S. Hillmansen and M. Chen, "Future of electric railways: advanced electrification systems with static converters for ac railways," IEEE Electrification Magazine, vol. 4, no. 3, pp. 6-14, Sept. 2016.

[12] M. Vasiladiotis, N. Cherix and A. Rufer, "Operation and control of single-to-three-phase direct ac/ac modular multilevel converters under asymmetric grid conditions," International Conference on Power Electronics and ECCE Asia (ICPE-ECCE), pp. 1061-1066, June 2015.

[13] L. Angquist, A. Haider, H. P. Nee, and H. Jiang, "Open-loop approach to control a modular multilevel frequency converter," European Conference on Power Electronics and Applications (EPE), pp. 1-10, Aug. 2011.

[14] L. Bessegato, K. Ilves, L. Harnefors, S. Norrga, and S. Ostlund, "Control and admittance modeling of an ac/ac modular multilevel converter for railway supplies," IEEE transactions on power electronics. vol.35, no. 3, pp. 2411-2423, July 2019.

[15] D. C. Ludois and G. Venkataramanan, "Simplified terminal behavioral model for a modular multilevel converter," IEEE Transactions on Power Electronics, vol. 29, no. 4, pp. 1622-1631, April 2014.

[16] A. Antonopoulos, L. Angquist and H.-P. Nee, "On dynamics and voltage control of the modular multilevel converter," European Conference on Power Electronics and Applications (EPE), pp. 1-10, Sept. 2009.

[17] H. Akagi, E. H. Watanabe and M. Aredes, "Generalized theory of instantaneous reactive power and its application," Hoboken, NJ, USA: Wiley, 2007.

[18] X. Yang, J. Li, X. Wang, W. Fan and T. Q. Zheng, "Circulating current model of modular multilevel converter," Asia-Pacific Power and Energy Engineering Conference (APPEEC), Mar. 2011, pp. 1-6.

[19] J. Lebre and E. H. Watanabe, "Fullbridge MMC control for hybrid HVDC systems," Brazilian Power Electronics Conference (COBEP), Nov. 2017, pp. 1-6.

[20] A. A. Elserougi, A. M. Massoud and S. Ahmed, "Power control of grid-connected high-gain boost full-bridge modular multilevel converter," Southern Power Electronics Conference (SPEC), Dec. 2017, pp. 1-5.

[21] R. Teodorescu, M. Liserre and P. Rodriguez, "Grid converters for photovoltaic and wind power systems," Hoboken, NJ, USA: Wiley, 2011.